ELSEVIER

Volume 180, Number 10, October 2007

JOURNAL OF SOLID STATE CHEMISTRY

www.elsevier.com/locate/jssc

CONTENTS

Abstracted/indexed in BioEngineering Abstracts, Chemical Abstracts, Coal Abstracts, Current Contents/Physics, Chemical, & Earth Sciences, Engineering Index, Research Alert, SCISEARCH, Science Abstracts, and Science Citation Index. Also covered in the abstract and citation database SCOPUS®. Full text available on ScienceDirect®.

Regular Articles

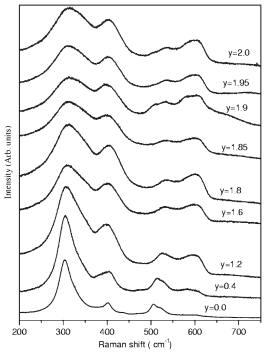

Raman spectra of $Nd_{2-y}Gd_yZr_2O_7$ with increasing proportion of Gd in $Nd_{2-y}Gd_yZr_2O_7$ series. A transition from ordered pyrochlore to disordered pyrochlore can be seen at $y \approx 1.8$.

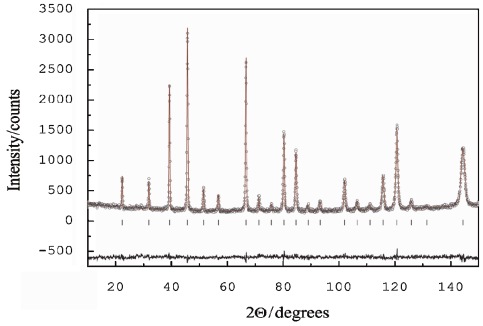

Oxynitrides of the general composition $SrMoO_{3-x}N_x$ ($x>1$) were synthesized by thermal ammonolysis of $SrMoO_4$. X-ray and neutron diffraction detect no deviation from the cubic symmetry for the samples. X-ray absorption spectroscopy shows evidence of local distortions of $Mo(O,N)_6$ octahedra. The resistivity values of the samples are higher and the Seebeck coefficient values are lower than those of $SrMoO_3$.

Regular Articles—Continued

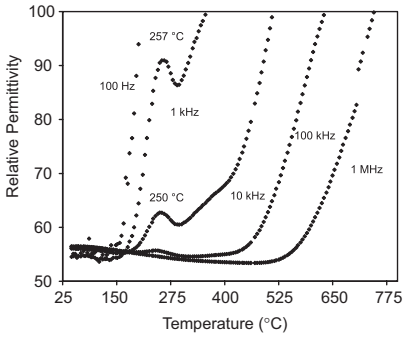

Temperature dependence of the relative permittivity of an Aurivillius-type $Bi_3Fe_{0.5}Nb_{1.5}O_9$.

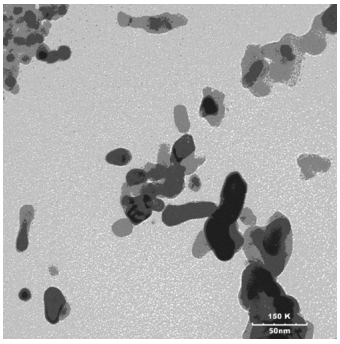

Transmission electron microscope (TEM) image of the fluorite-type Y_2O_3-doped CeO_2 (YCO) powder prepared by the reaction between proton conducting BCY and CO_2 in the temperature range 700–1000 °C.

Analysis of the electronic structure of $Hf(Si_{0.5}As_{0.5})As$ by X-ray photoelectron and photoemission spectroscopy
Andrew P. Grosvenor, Ronald G. Cavell, Arthur Mar and Robert I.R. Blyth
page 2670

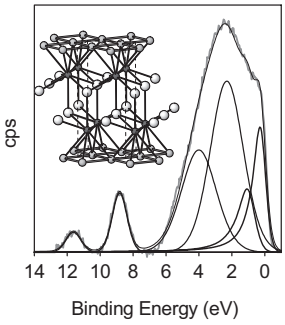

Fitted XPS valence band spectrum of $Hf(Si_{0.5}As_{0.5})As$, adopting the ZrSiS-type structure.

Evolution of titania nanotubes-supported WO_x species by *in situ* thermo-Raman spectroscopy, X-ray diffraction and high resolution transmission electron microscopy
M.A. Cortes-Jácome, C. Angeles-Chavez, M. Morales, E. López-Salinas and J.A. Toledo-Antonio
page 2682

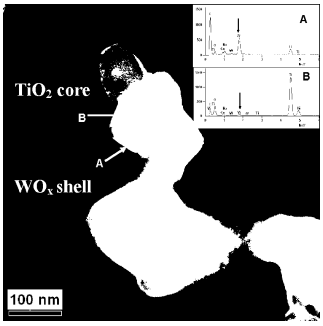

Titania nanotubes loaded with 15 wt% W atoms were characterized from room temperature (rt) to 1000 °C by thermo-Raman spectroscopy in N_2. At 1000 °C, a core–shell model material was obtained, with a shell thickness of *ca.* 5 nm composed by nanoclusters of sodium tungstate, and a core composed mainly of rutile TiO_2 phase.

Synthesis and crystal structure of $Bi_{6.4}Pb_{0.6}P_2O_{15.2}$ A new polymorph in the series $Bi_{6+x}M_{1-x}P_2O_{15+y}$
N. Arumugam, V. Lynch and H. Steinfink
page 2690

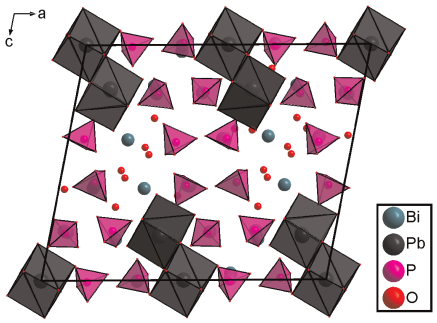

View of the structure of $Bi_{6.4}Pb_{0.6}P_2O_{15.2}$ parallel to the *b*-axis.

Surface chemistry and optical property of TiO_2 thin films treated by low-pressure plasma
Marshal Dhayal, Jin Jun, Hal Bon Gu and Kyung Hee Park
page 2696

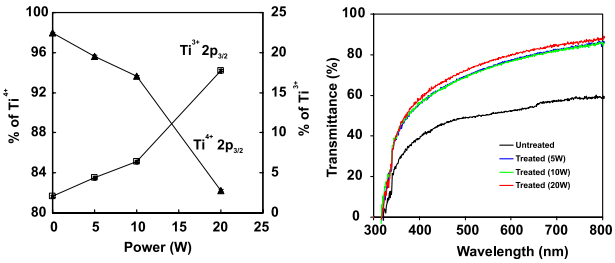

The surface chemistry and surface states of TiO_2 films was modified using low-pressure RF plasma treatment. The surface roughness and crystalline structure remain unchanged for low-pressure plasma-treated films. There was an increase in the Ti^{3+} surface states of Ti2*p* at the surface and this can be useful to increase the photocatalytic activities of TiO_2 films. The proportion of carbon atoms as carboxyl group in C1*s* was also increased after plasma treatment. All the plasma-treated films show a higher optical transmittance when untreated and it was increased when the power was increased. The increase in the optical transmission could be due to surface cleaning of films by plasma treatment and possibly due to change in the surface chemistry.

Next-nearest neighbour contributions to P $2p_{3/2}$ X-ray photoelectron binding energy shifts of mixed transition-metal phosphides $M_{1-x}M'_xP$ with the MnP-type structure
Andrew P. Grosvenor, Ronald G. Cavell and Arthur Mar
page 2702

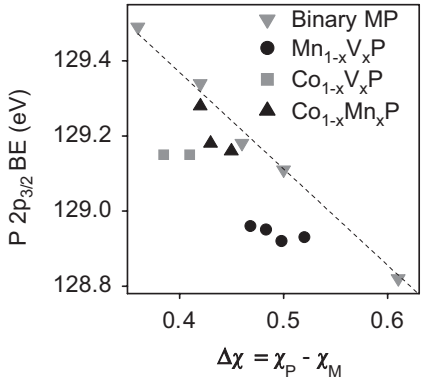

The mixed phosphides $Co_{1-x}Mn_xP$, $Mn_{1-x}V_xP$, and $Co_{1-x}V_xP$ with the MnP-type structure have been studied by use of XPS and XANES. The P 2*p* binding energies in the mixed phosphides display shifts relative to the binary phosphides that cannot be explained by interaction of the nearest neighbours alone.

Continued

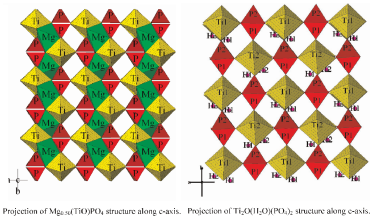

The structure of TiHP can be described as a $TiOPO_4$ framework constituted by chains of tilted corner-sharing $[TiO_6]$ octahedra and cross linked by $[PO_4]$ tetrahedra with empty cavities in the framework.

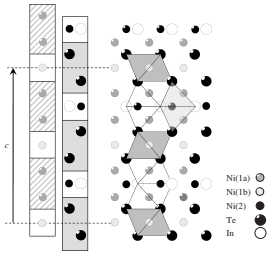

The crystal structure of $Ni_{3.31}InTe_2$ is a superstructure of the *NiAs* type structure with $\mathbf{q}=\gamma[0\,0\,1]^*$, $\gamma=2/3$. The -In/Te/Te/- stacking sequence at the hcp array can be described with a crenel function with the length of the atomic domains $\Delta^{Te}=\gamma$ and $\Delta^{In}=1-\gamma$. With decreasing In and Ni content, the modulation wave vector, γ, increases continuously until $\gamma=1$. The corresponding effect in real space is that the In layers separating double layers of Te occur less frequently until at $\gamma=1$ the CdI_2 type structure of $Ni_{1+x}Te_2$ is reached.

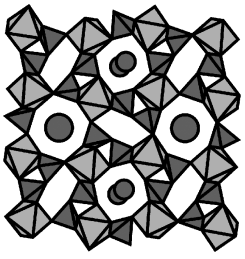

The $[Mo_8P_{16}O_{56}]\infty$ framework showing the two kinds of eight-sided tunnels able to accept univalent or divalent ions.

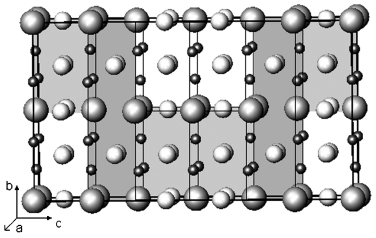

Two new compounds, $La_3Ru_8B_6$ and $Y_3Os_8B_6$, were synthesized by arc melting the elements. From room temperature X-ray single-crystal and powder diffraction, both compounds were found to be isotypic with $Ca_3Rh_8B_6$ compound (*Fmmm* space group (no. 69), $Z=4$) and their structures are built up from $CeCo_3B_2$-type and $CeAl_2Ga_2$-type structural fragments taken in ratio 2:1. They are the members of structural series $R(A)_nM_{3n-1}B_{2n}$ with $n=3$ (R is the rare earth metal, A the alkaline earth metal, and M the transition metal).

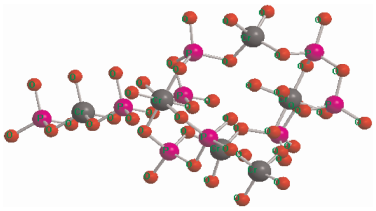

The optical absorption spectroscopic studies on Li_2O–CaF_2–P_2O_5: Cr_2O_3 glass ceramics indicate that a part of Cr^{3+} ions oxidized into Cr^{6+} ions during the crystallization. These ions enter the glass network with CrO_4^{2-} structural units, alternate with PO_4 units and increase the rigidity of the glass-ceramic sample.

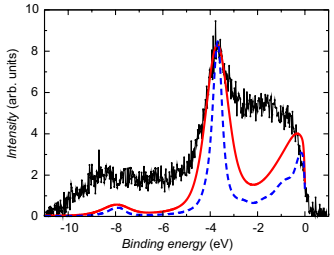

Comparison of the experimental valence band corrected by the background (thin line with crosses) with the theoretical spectra. These latter were convoluated by Lorentzians with a full-width-half-maximum (FWHM) of 0.4 eV (dashed line) or by the pseudoVoigt profile function with a FWHM of 0.8 eV and 0.5 eV for the Lorentzian and Gaussian components, respectively (solid line).

Phase stabilities of monoclinic oxoborates LaB_3O_6 and GdB_3O_6 in *C*121 and *I*12/*a*1 phase—Energetics and chemical bonds derived from first-principles calculations

Jun Yang and Michael Dolg

page 2763

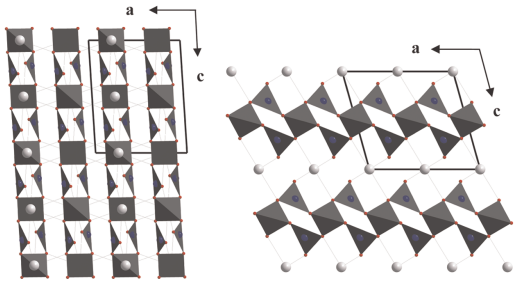

The electronic structures, energetics and metal–oxygen chemical bonds have been calculated for both monoclinic phases in the space groups of centrosymmetric *I*2/*a* (left) and noncentrosymmetric *C*2 (right) for LaB_3O_6 and GdB_3O_6, respectively, by the gradient corrected hybrid density functional theory.

Lamellar structures in neodymium borides

L. Kienle, V. Babizhetskyy, V. Duppel, R. Guérin and A. Simon

page 2775

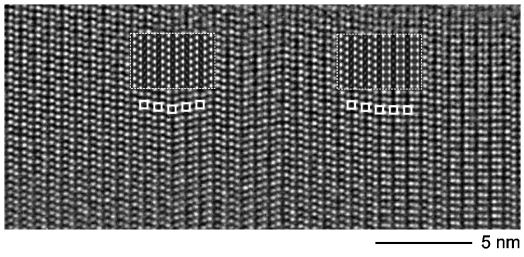

The lamellar real structure of neodymium borides made visible by HRTEM.

Formation of tetragonal hydrogen tungsten bronze by reactive mechanical alloying

G. Urretavizcaya, F. Tonus, E. Gaudin, J.-L. Bobet and F.J. Castro

page 2785

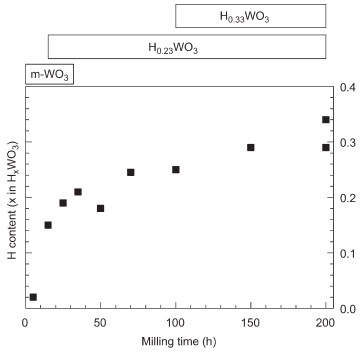

Hydrogen tungsten bronzes have been synthesized by reactive mechanical alloying (RMA) monoclinic WO_3 under H_2 atmosphere. By using two milling devices with different energy ranges a similar phase evolution with distinct reaction times was observed. The materials were characterized by XRD, SEM, DSC and total hydrogen content determination. The final product obtained was a mixture of tetragonal $H_{0.33}WO_3$ and $H_{0.23}WO_3$ bronzes.

Hydrated surface structure and its impacts on the stabilization of *t*-ZrO_2

Hui Wang, Guangshe Li, Yanfeng Xue and Liping Li

page 2790

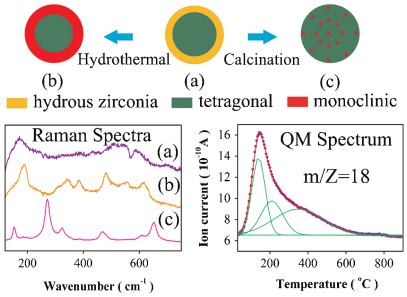

Surfaces of *t*-ZrO_2 were terminated by hydration layers, which completely transformed into *m*-ZrO_2 when treating at high hydrothermal temperatures. Alternatively, hydration layers transformed into *t*-ZrO_2 when annealing at $T<700$ °C. *t*-ZrO_2 partially transformed into *m*-ZrO_2 in both bulk and surface regions at $T>700$ °C.

Crystal structures and dielectric properties of ordered double perovskites containing Mg^{2+} and Ta^{5+}

Young-Il Kim and Patrick M. Woodward

page 2798

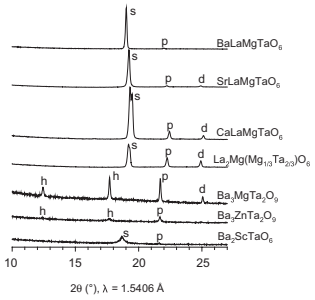

XRPD patterns at low angle range for the Mg/Ta complex perovskite oxides, showing various origins of diffraction planes: s—rock-salt type cation ordering, h—1:2 cation ordering, p—primitive cube edge, and d—octahedral tilting.

Physicochemical compatibility of $SrCeO_3$ with potential SOFC cathodes

J. Tolchard and T. Grande

page 2808

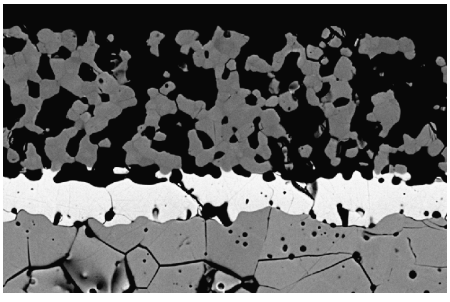

Assessment of the $SrCeO_3$ proton conductor shows this material to have poor chemical compatibility with La*M*O_3 perovskite systems, but predicts coexistence with Ruddlesden-Popper type oxides.

Continued

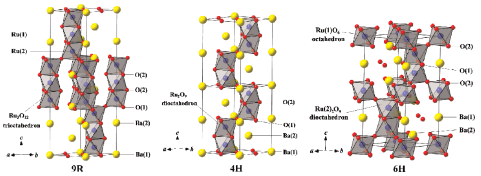

The single-phase 6H $BaRuO_3$ was synthesized under high pressure high temperature. The electrical resistivity of 6H $BaRuO_3$ follows a $T^{3/2}$ relation below 60.0 K. Both magnetic susceptibility and specific heat data indicate that 6H $BaRuO_3$ is an exchange-enhanced Pauli paramagnet with the large Wilson ratio and Stoner enhancement factor.

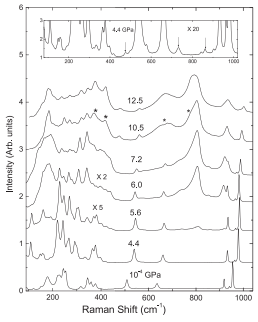

Raman spectra of α-$NaVO_3$ at different pressures. Spectrum in the range 90–460 cm^{-1} have a scale factor of 5–5.6 GPa, and thereafter a factor of 2. Inset shows the appearance of weak peaks above 4.4 GPa. *Indicates the modes which increase in intensity above 9 GPa.

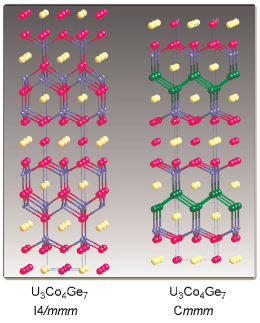

A new uranium compound, $U_3Co_2Ge_7$ has been synthesized and structurally characterized. The close structural relationship between the orthorhombic structure of $U_3Co_2Ge_7$ and the tetragonal structure of $U_3Co_4Ge_7$ is emphasized. $U_3Co_2Ge_7$ is a moderate heavy-fermion ferromagnet (or ferrimagnet) at 40 K that undergoes another transition at 20 K.

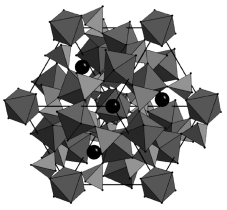

Polyhedron view of $K_{1.96}Mn_{0.57}Zr_{1.43}(PO_4)_3$ along [111] direction. [MO_6] octahedra—blue, [PO_4] tetrahedra—purple, potassium cations—black circles.

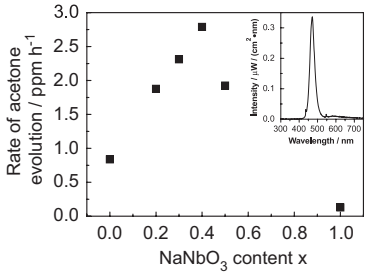

A series of orthorhombic photocatalysts $(AgNbO_3)_{1-x}(NaNbO_3)_x$ solid solutions have been synthesized by a solid-state reaction method. The composition dependence of the photophysical and photocatalytic properties of synthesized solid solutions has been investigated systematically. The solid solutions show higher visible-light photocatalytic activities for gaseous IPA decomposition in comparison with $AgNbO_3$, although the light intensity is 0.01 mW cm^{-2}. Rate of acetone evolution under visible-light irradiation as a function of $NaNbO_3$ content in $(AgNbO_3)_{1-x}(NaNbO_3)_x$. The inset is the spectrum of BLEDs. The light intensity is 0.01 mW cm^{-2}.

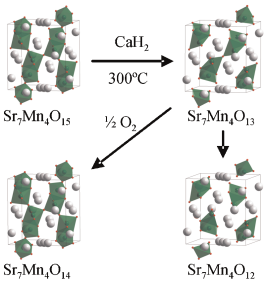

Topotactic reduction of $Sr_7Mn_4O_{15}$ selectively removes apex-linked oxide ions.

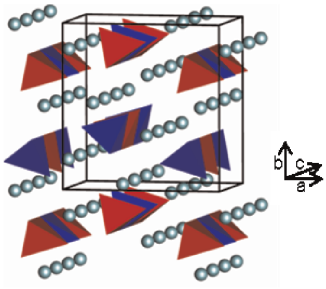

Neutron powder diffraction has been used to prove that Ba_2CoS_3 shows long-range antiferromagnetic order at low temperatures, despite the quasi-one-dimensional arrangement of the CoS_4 tetrahedra in the crystal structure.

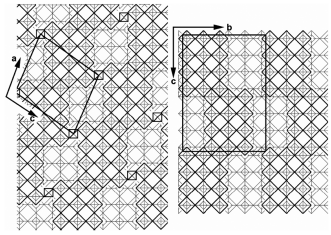

The crystal structure of $Nb_{22}O_{54}$ is reported, and the structure of orthorhombic $Nb_{12}O_{29}$ is reexamined. Bond valence sums do not show the presence of charge ordering, suggesting that all 4*d* electrons are delocalized in these compounds at $T = 200$ K, despite the well-known magnetic behavior of these materials.

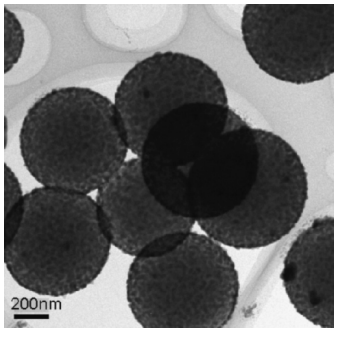

Silica–silver core–shell composite particles with uniform thin silver layers are prepared by a facile and one-step ultrasonic electrodeposition method. Moreover, the continuity of Ag distribution, the surface roughness and the thickness of silver layer are controllable. Optical properties of the composite particles with different silver content were also investigated.

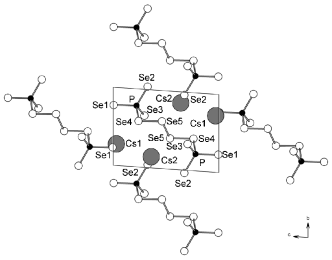

The new compound $Cs_4P_2Se_{10}$ was discovered following a high-temperature *in situ* synthesis in the NMR spectrometer and the structure was determined by single-crystal X-ray diffraction. It contains the new $[P_2Se_{10}]^{4-}$ anion.

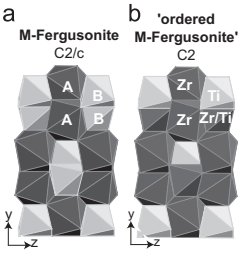

Crystal structure of zirconium titanate with 27.5–35 mol% TiO_2. (a) As refined in present study with M-fergusonite structure, with site *A* occupied predominantly with Zr, and site *B* with a random mix of Ti and Zr. (b) Actual cation ordering pattern of this compound as indicated by superstructure reflections, resulting in the splitting of site *B* into two distinct sites.

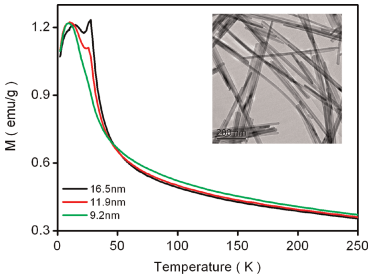

Highly crystalline one-dimensional (1D) α-MnO_2 nanostructures were achieved to have tunnel structures modified by NH_4^+ species and water molecules. By tuning the diameters. 1D α-MnO_2 showed two magnetic transition as indicated by hump and kink peaks at low temperatures. Mn ions presented in 1D α-MnO_2 were determined to be in a mixed valency of high spin state Mn^{4+}/Mn^{3+}.

Continued

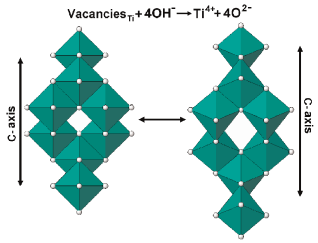

Cobaltiferous titania photocatalysts calcined at 200 °C contain up to 16 at% metal vacancies (V) and are significantly amorphous (up to 53 wt%). The presence of metal vacancies can be monitored by following the dilation of the '*c*' lattice parameter as the crystallite size increases during calcination.

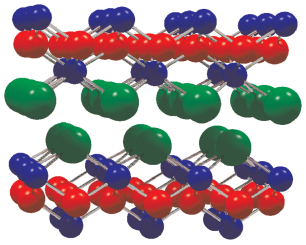

Very rapid, filament-initiated metathesis reactions between two solids, metal trihalides and Na_2O_2, lead to crystalline metal oxyhalides in seconds. All products crystallize in the PbFCl structure (BiOCl shown). In addition to single metal *M*OCl (Bi, La, Sm, Gd) and BiOI systems, solid-solution $Gd_xSm_{1-x}OCl$ materials are also rapidly accessible using this reactive precursor strategy.

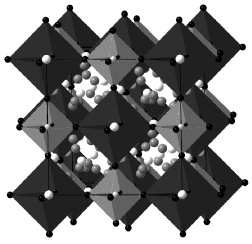

The new compounds $U_6Fe_{16}Si_7$ and $U_6Fe_{16}Si_7C$ crystallize with the ternary ordered variant of the Th_6Mn_{23} type, commonly referred as $Mg_6Cu_{16}Si7$ and with a novel "filled" variant of this type of structure, respectively.

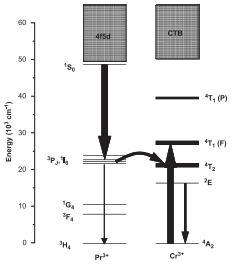

The Cr^{3+} ion was chosen as a co-dopant to modify the photon cascade emission properties of $CaAl_{12}O_{19}$: Pr via energy transfer. The cascade emission process and the energy transfer mechanisms were systemically investigated. The drawback for $CaAl_{12}O_{19}$: Pr, Cr as a practical VUV phosphor was also discussed.

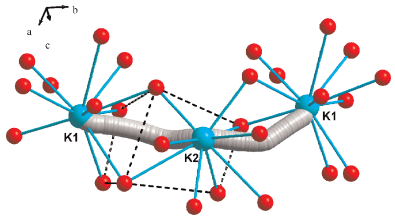

Optimized trajectory for K1–K2–K1 jump as determined by BVS analysis.

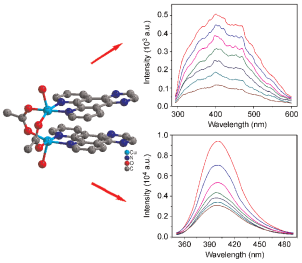

Poor water-soluble copper(II) complexes constructed from dipyrido[3,2-*d*:2′,3′-*f*]quinoxaline ligand have been synthesized and structurally characterized by single-crystal X-ray diffraction analyses. The complexes were used to fabricate the highly ordered multilayer films by layer-by-layer (LBL) self-assembly methods. The fluorescent properties of the films were studied and the results showed that the forming condition of films have great influence on their properties.

Continued

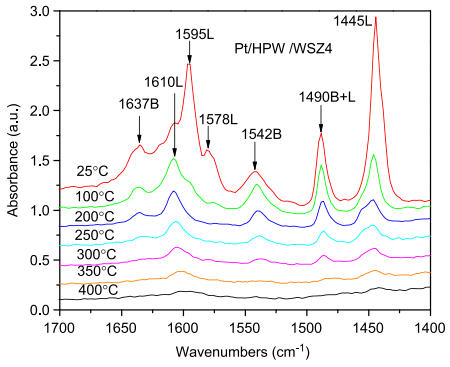

Modifications of the surface and framework of Si-MCM-41 by depositing a heteropolyacid on the surface and by introducing foreign Zr^{4+} ions into the framework are investigated. Brönsted acidity of the $Pt/H_3PW_{12}O_{40}$/Zr-MCM-41 catalysts was greatly enhanced by 2–10 times relative to the bare Zr-MCM-41 support.

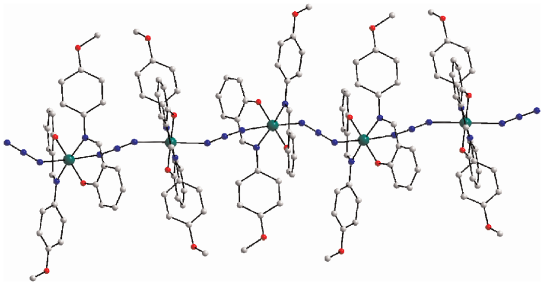

A novel azido-bridged manganese(III) complex with bidentate Schiff base ligands has been prepared and characterized structurally and magnetically. The complex is of one-dimensional chain structure with single end-to-end azido bridges in axial positions. Two bidentate Schiff base ligands coordinate in the equatorial mode. The magnetic measurements show that the complex exhibits weak antiferromagnetic interaction.

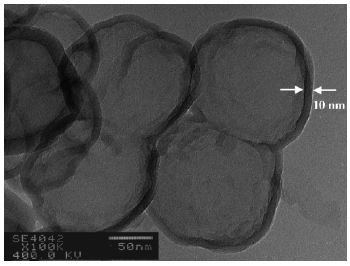

TEM micrograph of the hollow silica particles. Wall thickness, as estimated by TEM from the ring around the perimeter of the hollow spheres, was ~10 nm. TEM micrographs of hollow silica spheres show that the sphericity of the core Fe_2O_3 was preserved.

Rapid Communications

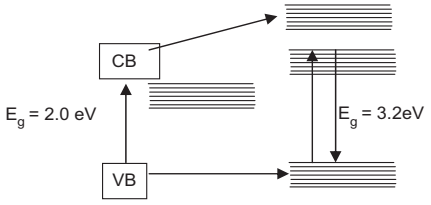

Photocatalytic mechanism of the polymer composite with titania. A new heterogeneous conducting polymer composite with titania (P3HT/TiO_2) was synthesized and the photocatalytic activity this composite was investigated by degrading a common dye under UV exposure. It was shown that the nanocomposite exhibited synergetic photocatalytic catalytic activity compared to either the polymer or TiO_2 alone. The scheme of the possible mechanism of enhancement of photocatalytic degradation rate in a conducting polymer nanocomposite is shown in the figure.

Corrigendum

Author inquiries

Submissions

For detailed instructions on the preparation of electronic artwork, consult the journal home page at http://authors.elsevier.com.

Other inquiries

Visit the journal home page (http://authors.elsevier.com) for the facility to track accepted articles and set up e-mail alerts to inform you of when an article's status has changed. The journal home page also provides detailed artwork guidelines, copyright information, frequently asked questions and more.

Contact details for questions arising after acceptance of an article, especially those relating to proofs, are provided after registration of an article for publication.

Language Polishing

Authors who require information about language editing and copyediting services pre- and post-submission should visit http://www.elsevier.com/wps/find/authorshome.authors/languagepolishing or contact authorsupport@elsevier.com for more information. Please note Elsevier neither endorses nor takes responsibility for any products, goods, or services offered by outside vendors through our services or in any advertising. For more information please refer to our Terms & Conditions at http://www.elsevier.com/wps/find/termsconditions.cws_home/termsconditions.

For a full and complete Guide for Authors, please refer to *J. Solid State Chem.,* Vol. 180, Issue 1, pp. *bmi–bmv*. The instructions can also be found at http://www.elsevier.com/wps/find/journaldescription.cws_home/622898/authorinstructions.

Journal of Solid State Chemistry has no page charges.